AJG

Article

Assessment of Orbital Interpolation Methods for Accurate Baseline Estimation in InSAR Applications

Tsung-Han Wen*[1], Tee-Ann Teo[1], K.H. Hsu[2], M.C. Wu[2], Y.S. Lee[2]

[1]National Yang Ming Chiao Tung University
1001 University Road, Hsinchu, Taiwan

Email: edwen.en08@nycu.edu.tw, tateo@nycu.edu.tw

[2]Taiwan Space Agency (TASA),
8F, 9 Prosperity 1st Road, Hsinchu Science Park, Hsinchu, Taiwan

Email: khhsu@tasa.org.tw, momo@tasa.org.tw, sunnylee@tasa.org.tw

*Corresponding author: T-H Wen edwen.en08@nycu.edu.tw

Received: November 10, 2023; Accepted: March 15, 2024; Published: April 15, 2024

ABSTRACT

Interferometric synthetic aperture radar (InSAR) is a technique to measure ground deformation and topographic changes with high precision. Accurate estimating of the baseline between two orbits, which refers to the satellite's relative position in space during radar image acquisition, is crucial for obtaining reliable InSAR measurements. However, the discrete orbital trajectory of the satellite requires interpolation to obtain the position and velocity at arbitrary times. This research investigates the impact of different orbital interpolation methods on the accuracy of baseline estimation in InSAR applications. Since the advanced SAR satellites have centimeter-level accuracy through precise orbit determination, interpolation-induced errors play a critical role in baseline estimation. This study compares different orbital interpolation methods, including linear, cubic, piecewise cubic, and Lagrange interpolations. We analyze the results of various interpolation techniques and assess their influence on baseline estimation. The experiment utilized 21 TerraSAR-X and TanDEM-X images to calculate the perpendicular baseline between orbits. The calculated baselines were compared with ESA SNAP software, and the mean difference was less than 1.7m. The cubic interpolation showed better results than the other three methods. The findings provide valuable insights into selecting the most suitable interpolation method for accurate baseline estimation in different scenarios, contributing to improved InSAR data processing and interpretation.

Keywords: InSAR, baseline, orbital interpolation

1. INTRODUCTION

Earth resources satellites typically record the satellite's ephemeris discretely in metadata. However, most satellite data processing requires continuous and precise orbital information. Therefore, orbital interpolation is an essential procedure. It is particularly critical for missions that demand high-precision orbital data, such as high-resolution optical imaging satellites that require direct georeferencing (Teo, 2011) and radar sensors used in Interferometric Synthetic Aperture Radar (InSAR) missions (Fattahi and Amelung, 2014), as discussed in this study. The InSAR technique utilizes the phase difference of radar signals, providing a non-contact, high-precision method for measuring critical geophysical parameters, such as the topography height or ground deformation. Due to its capability to provide all-weather, wide-area observation data, space-borne InSAR is currently extensively utilized in Earth environmental monitoring (Chaussard et al., 2014; Li et al., 2019; Kang et al., 2021).

InSAR baseline calculation plays a pivotal role in the assessment of radar interferometry. For instance, in the process of calculating surface deformation using Differential Interferometric Synthetic Aperture Radar (D-InSAR), the selection of image pairs is mainly based on the baseline (Reigber et al., 1997; Li et al., 2022). Similarly, when deriving surface elevation through InSAR, errors in the baseline can directly impact the resulting elevation. Orbital error can lead to baseline error, which subsequently affects elevation error. Theoretically, a longer perpendicular baseline results in reduced elevation error. However, as the perpendicular baseline increases, the correlation between two radar images weakens, which is disadvantageous for calculating the interferometric phase (Hanssen, 2001; Lu et al., 2018).

Obtaining precise InSAR measurements relies heavily on accurately determining the orbit and baseline (Osmanoğlu et al., 2016), which represents the satellite's relative position in space during radar image acquisition. However, due to the discrete recording of the satellite's orbital trajectory, interpolation is necessary to calculate its position and velocity at arbitrary times (Breit et al., 2009; Fan et al., 2019). In recent years, with the continuous advancement of SAR satellites, the orbital accuracy has steadily improved, exemplified by satellites such as TerraSAR-X (Hong et al., 2017) and Kompsat-5 (Lee et al., 2022), which achieve centimeter-level orbital accuracy. The enhancement in orbital accuracy has also resulted in a relatively increased impact caused by orbital interpolation. For example, the accuracy of the TerraSAR-X precise orbit was 12mm to 17mm (Hackel et al., 2018), the time interval for orbital state vector in Terra SAR-X metadata is 10 sec, and the distance between these two sampling points is about 76km. Therefore, the interpolation-induced error has to be

considered in the InSAR process. Previous studies have examined the accuracy impact of interpolation methods, such as Vassilaki and Stamos (2014), who investigated the influence of various interpolation methods on the orbital accuracy of TerraSAR-X. However, most research (Schenewerk, 2003; Yousif and El-Rabbany, 2007) has focused solely on orbital accuracy without further considering its effects on the baseline, which is one of the important factors for InSAR process.

The sources of error in baseline estimation can be categorized into GNSS measurement errors and baseline transformation errors. The GNSS measurement errors encompass factors such as satellite clock inaccuracies, atmospheric effects (e.g., tropospheric and ionospheric delays), receiver noise, and biases. The baseline transformation errors involve errors in orbit interpolation methods, sampling intervals, and the conversion errors between the antenna phase center and satellite center to the geodetic coordinate system. This study investigates the impact of various orbital interpolation methods on the accuracy of baseline estimation in InSAR applications. Furthermore, experimental analysis was conducted utilizing twin SAR satellites, TerraSAR-X and TanDEM-X. The paper is structured as follows: Section 2 introduces the methodology for calculating perpendicular baselines and discusses different orbital interpolation methods. Section 3 presents the experimental results and discussions, while Section 4 summarizes the study's outcomes and provides recommendations.

2. METHODOLOGY

The objective of this study is to comprehensively investigate the impact of various orbital interpolation methods on the estimation of perpendicular baselines in SAR image pairs. Before calculating the perpendicular baseline, we analyze the perpendicular baseline errors propagated to subsequent InSAR applications. Taking the calculation of surface height using phase differences from SAR image pairs as an example: Two SAR orbits distance represented by baseline B and they acquire the complex response at range R_1, the change in look angle can be inferred from the interferometric phase, as illustrated in Figure 1. By utilizing the range R_1 and the height of the platform (H_{sat}), it becomes feasible to calculate the height of point P (H_P). To understand the impact of baseline errors on elevation estimation, we differentiate $B_\perp$ in Equation 1, resulting in Equation 2. After rearrangement, Equation 3 establishes the relationship between σ_H, σ_B and the initial elevation (H_0). It conclude that σ_H is inversely proportional to $B_\perp$, indicating that shorter perpendicular baselines lead to larger elevation errors, whereas longer perpendicular baselines result in smaller elevation errors. In other words, orbital error leads to baseline error (σ_B), which in turn affects the elevation error (σ_H).

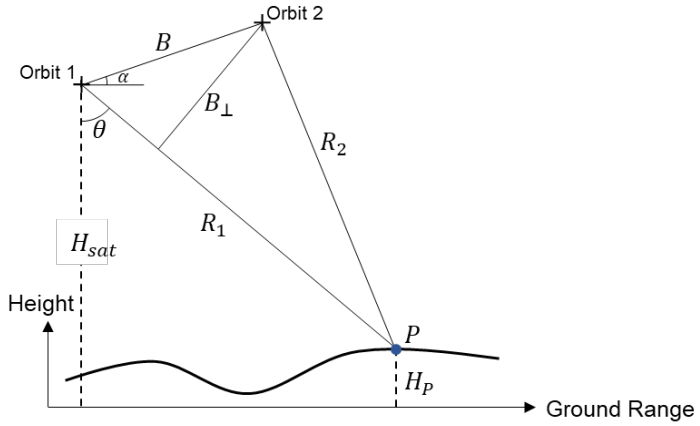

Figure 1. Interferometric configuration for height derivation.

$$H = -\frac{\lambda R sin\theta}{4\pi B_\perp}\partial\varphi \quad (1)$$

$$\sigma_H = \frac{\partial H}{\partial B_\perp} = \frac{\lambda R sin\theta}{4\pi (B_\perp)^2}\partial\varphi * \sigma_{B_\perp} \quad (2)$$

$$\sigma_H = \frac{-\lambda R sin\theta}{4\pi B_\perp}\partial\varphi \frac{-\sigma_{B_\perp}}{B_\perp} = H_0 \frac{-\sigma_{B_\perp}}{B_\perp} \quad (3)$$

where $H =$ object height
$H_0 =$ initial object height
$\lambda =$ wavelength
$R =$ slant range
$\theta =$ look angle
$B_\perp =$ perpendicular baseline
$\sigma_{B_\perp} =$ standard deviation of perpendicular baseline
$\partial\varphi =$ interferometric phase change

Based on the concise analysis above, it can be concluded that the perpendicular baseline is a crucial parameter in InSAR applications. The following two subsections will separately elaborate on the methodology employed in this study for calculating the perpendicular baseline and the orbit interpolation method utilized.

2.1 Perpendicular Baseline Calculation

The calculation of the perpendicular baseline ($B_\perp$) involves first determining the three-dimensional coordinates (P_1, P_2, and P), where P_1 corresponds to the master image's orbit, P_2 to the slave image's orbit, and P to the ground point. (Figure 2). The entire process consists of three steps: firstly, it is necessary to determine whether there is an overlap

between the master and slave images. The calculation of the baseline is only required when there is an overlap between corresponding image pairs. Therefore, the four corner coordinates of the two images in object space are utilized to calculate the overlap extent, and the baseline is only computed when the overlapping ratio exceeds 50%.

The second step involves computing the position of the slave image, P_2, within its orbit. The position of the master image in object space, as well as the three-dimensional coordinates of the corresponding P_1 point in the orbit and the velocity vector in the normal direction, can be obtained from ephemeris. Subsequently, by utilizing two conditions: (1) the coplanarity condition among P_1 from Orbit 1, P_2 from Orbit 2, and the ground point P, and (2) the requirement that P_2 lies on the slave image's orbit, we can establish the orthogonality condition (Equation 4) and the collinearity equation (Equation 5). Substituting Equation 5 into Equation 4 yields Equation 6, from which we can solve for the scale factor s. Using Equation 5 with the determined scale factor s, we can then obtain the position of the slave image's P_2 point within its orbit.

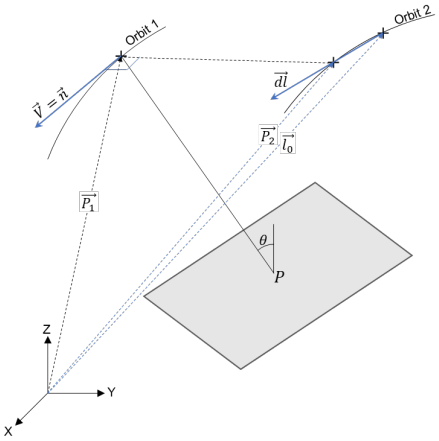

Figure 2. Illustration of orbit geometry.

$$\left(\overrightarrow{P_2} - \overrightarrow{P_1}\right) \cdot \vec{n} = 0 \tag{4}$$

$$\overrightarrow{P_2} = \overrightarrow{l_0} + \overrightarrow{dl} \times s \tag{5}$$

$$\left(\left(\overrightarrow{l_0} + \overrightarrow{dl} \times s\right) - \overrightarrow{P_1}\right) \cdot \vec{n} = 0 \tag{6}$$

where $\overrightarrow{P_1} = (X_s, Y_s, Z_s)$

$\vec{n} = \left(V_{X_s}, V_{Y_s}, V_{Z_s}\right)$

$\overrightarrow{l_0} = (X_s', Y_s', Z_s')$

$\overrightarrow{dl} = \left(d_{X_s}', d_{Y_s}', d_{Z_s}'\right)$

In the third step, subtracting the position vector of the slave image's $\overrightarrow{P_2}$ from the position vector of the master image's $\overrightarrow{P_1}$ yields the baseline vector $\vec{B}$ (Equation 7). By utilizing the position vector of the ground point $\vec{P}$, we can calculate the vector $\vec{d}$ between the orbit and the ground point (Equation 8). Subsequently, employing Equation 9 to calculate the area of the parallelogram $\square abcd$ and utilizing an area identity equation, we obtain Equation 10. The parallelogram $\square abcd$ is constructed from the coordinates of two orbital points and the ground point, as illustrated in Figure 3 (i.e., the red line). Finally, Equation 11 can be derived through transposition, allowing for determining the perpendicular baseline length.

In the previous step, we obtained the length of the perpendicular baseline, but it lacks directional information. Therefore, it is necessary to use azimuth angles to determine the sign (positive or negative) of the perpendicular baseline. We calculate the azimuth angles φ_{OM}, φ_{OL}, and φ_{OR}, all measured clockwise from the north direction. Here, φ_{OM} corresponds to the azimuth angle from the scene center to the master image, while φ_{OL} and φ_{OR} are the azimuth angles from the scene center to the left-side and right-side slave images, respectively (Figure 4). This implies that when slave orbit is on the right side of the master orbit's direction, perpendicular baseline is positive. Conversely, when slave orbit is on the left side of the master orbit's direction, perpendicular baseline is negative.

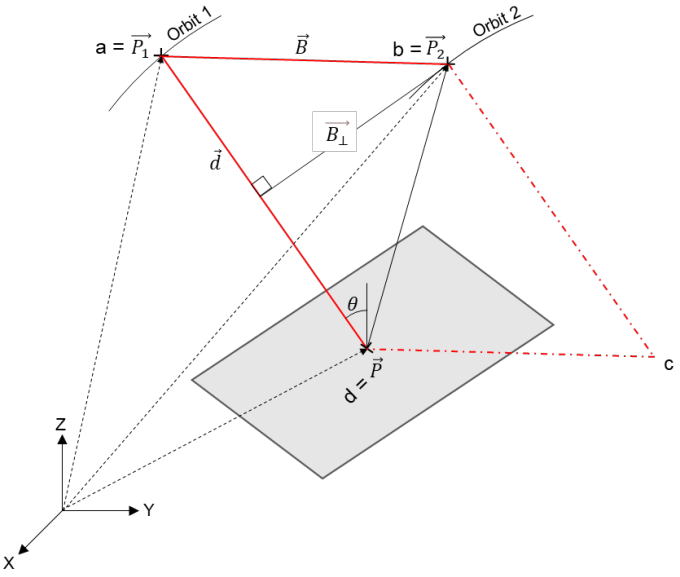

Figure 3. Configuration of perpendicular baseline.

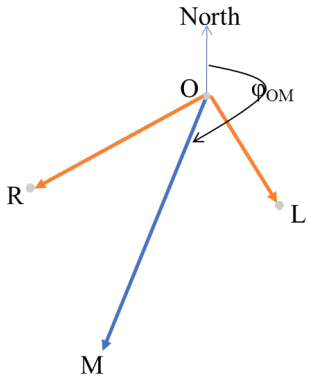

Figure 4. Diagram illustrating the sign of the perpendicular baseline.

$$\vec{B} = \overrightarrow{P_2} - \overrightarrow{P_1} \quad (7)$$

$$\vec{d} = \vec{P} - \overrightarrow{P_1} \quad (8)$$

$$Area_{\square\, abcd} = \left|\vec{B} \times \vec{d}\right| = \left|\overrightarrow{B_\perp}\right| \cdot \left|\vec{d}\right| \quad (9)$$

$$\left|\vec{B} \times \vec{d}\right| = \left|\overrightarrow{B_\perp}\right| \cdot \left|\vec{d}\right| \quad (10)$$

$$\left|\overrightarrow{B_\perp}\right| = \frac{\left|\vec{B} \times \vec{d}\right|}{\left|\vec{d}\right|} \quad (11)$$

where, $\vec{B}$ is the baseline between points P_1 and P_2; $\vec{d}$ is a vector between points P_1 and P; $\left|\overrightarrow{B_\perp}\right|$ is the length of perpendicular baseline.

2.2 Orbit Interpolation Methods

This study employs four interpolation methods to interpolate orbit: linear, cubic, piecewise cubic, and Lagrange interpolations. The parameters subject to interpolation include the satellite's position (X_s, Y_s, Z_s) and velocity ($V_{X_s}, V_{Y_s}, V_{Z_s}$). The following formulas are provided as examples, focusing solely on the interpolation of the X_s.

2.2.1 Linear interpolation

Llinear interpolation involves approximating the sensor's orbit between 2 timestamps as a straight-line segment. Utilizing sensor positions and velocities at 2 timestamps within the ephemeris, linear interpolation parameters can be calculated separately ($X_s, Y_s, Z_s, V_{X_s}, V_{Y_s}, V_{Z_s}$), with each parameter being computed from 2 unknown coefficients (shifting and direction) (Equation 12). Linear interpolation is a simple and intuitive method applicable for predicting missing values in sampled intervals under constant rate conditions. It is noteworthy that this method heavily relies on the distribution of data, thus may not adequately capture non-linear variations or abrupt changes in the data (Lepot et al., 2017).

$$X_s(t) = a_0 + a_1 t \quad (12)$$

2.2.2 Cubic Interpolation

Cubic interpolation assumes that the sensor's trajectory between two timestamps can be approximated using Cubics. In this approach, the data is segmented, and each segment is represented using a 3rd degree polynomial, effectively dividing the data into sections, with each section approximated by a cubic polynomial. Each segment is associated with four coefficients, as represented by Equation 13. The cubic interpolation requires at least 3 points and it is C1 continuity. The cubic method, similar to linear interpolation, involves the creation of a polynomial function between two points rather than a straight line. It estimates intermediate values along the way through the polynomial to consider trends over a larger range. Under the assumption of not emphasizing orbit accuracy, cubic splines can yield computationally efficient interpolation results (Neta et al., 1996 & Yousif and El-Rabbany, 2007).

$$X_s(t) = a_0 + a_1 t + a_2 t^2 + a_3 t^3 \quad (13)$$

2.2.3 Piecewise Cubic Hermite Interpolating Polynomial (PCHIP)

PCHIP interpolation also utilizes cubic polynomial segments, but unlike Cubic interpolation, it places a strong emphasis on preserving shape and smoothness between data points. In PCHIP interpolation, a local cubic polynomial is constructed at each data point, ensuring that these polynomials preserve both the values and the first derivatives of the data points. This guarantees smoothness between data points and exact interpolation at data points. The theoretical foundation of PCHIP interpolation incorporates principles from Hermite interpolation and piecewise interpolation. It determines the coefficients of each local cubic polynomial by calculating the slope between two adjacent data points (Rabbath and Corriveau, 2019). The cubic interpolation requires at least 4 points and it is C1 continuity.

2.2.4 Lagrange Interpolation

Lagrange interpolation is widely used in orbital interpolation (Feng and Zheng, 2005; Hu and Fang, 2009; Pustoshilov et al., 2017). This method assumes that the trajectory of the sensor can be approximated by a polynomial of degree (n-1) between each pair of coordinates. The Lagrange formula is an algebraic expression used to fit a specific dataset to a polynomial (with a degree equal to the number of data points), providing the exact value of that polynomial at each data point. Let $X_0, X_1, X_2, \ldots, X_n$ represent the values of the given data at times $t_0, t_1, t_2, \ldots, t_n$, respectively. The estimated value of X at any given time t, represented as $X_s(t)$, is expressed as follows (Yousif and El-Rabbany, 2007):

$$X_s(t) = a_0 X_0 + a_1 X_1 + a_2 X_2 + \cdots + a_n X_n = \sum_{i=0}^{n} a_i X_i \quad (14)$$

where $a_i = \frac{(t-t_0)(t-t_1)\ldots(t-t_{i-1})(t-t_{i+1})\ldots(t-t_n)}{(t_i-t_0)(t_i-t_1)\ldots(t_i-t_{i-1})(t_i-t_{i+1})\ldots(t_i-t_n)}$

3. EXPERIMENTS AND RESULTS

3.1 Dataset

In this study, a total of 21 radar images were employed, comprising 14 TerraSAR-X (TSX) and 7 TanDEM-X(TDX) acquisitions. TSX and TDX are German radar satellites equipped with X-band antennas, operated by DLR (German Aerospace Center). TSX was launched in 2007, while TDX joined the radar satellite constellation in 2010. The study area is located in the northern region of Taiwan, characterized by significant height overlap between image pairs (Figure 5). The orbital state vectors for TSX and TDX is precise orbit and the time interval for orbital state vectors is 10 seconds.

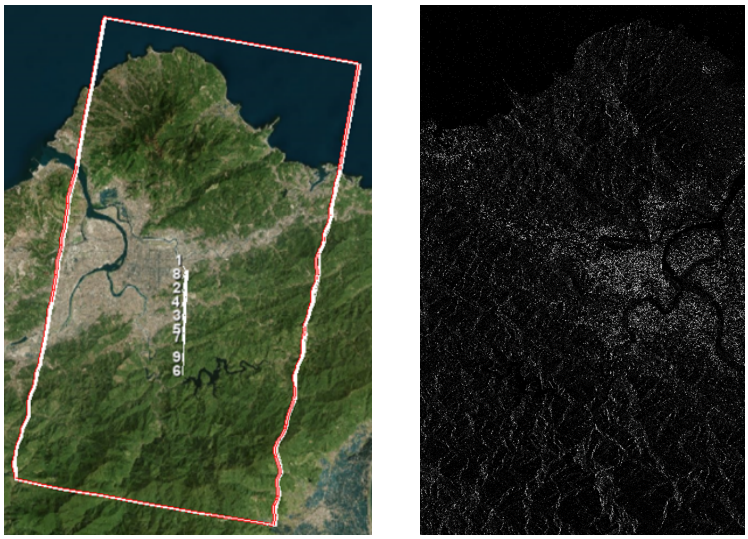

(a) (b)

Figure 5. The study area and schematic representation of SAR images. Figure 5(a) illustrates the locations where the images were acquired, while Figure 5(b) a showcase of SAR image captured on September 8, 2017.

3.2 Impact of Interpolation Methods on Orbit Position

The section involves data analysis using a single master image, and the calculated orbital positions using four different interpolation methods are presented in Table 1, with standard deviations in the three-axis directions exceeding 2.6 meters. However, the experimental precise orbit accuracy for TSX and TDX used in this study is better than 10 centimeters, indicating a relatively significant orbit error introduced by the interpolation methods. Figure 6 illustrates the distribution of orbital positions, with three subplots representing the X-Y plane, X-Z plane, and Y-Z plane, respectively. The black crosshairs denote the mean values

obtained from the four methods, while the black circles represent the 10-centimeter orbit accuracy tolerance. Furthermore, the linear interpolation method yields significantly different orbital positions compared to the other three methods. To assess whether there is a significant orbit error among the remaining three interpolation methods, we exclusively calculated Cubic, PCHIP, and Lagrange, obtaining the results presented in Table 2. The results indicate that these three interpolation methods show more significant errors in the X-direction, approximately 17 centimeters. In the Y and Z directions, the errors are less than 10 centimeters, but even the smallest Z-direction orbit error accounts for approximately one-fourth of the 10cm orbit accuracy.

Table 1. The interpolated orbit from four interpolation methods.

	X(m)	Y(m)	Z(m)
Linear	-3555956.259	5165813.525	2841952.161
Cubic	-3555964.607	5165824.265	2841958.182
PCHIP	-3555964.983	5165824.355	2841958.168
Lagrange	-3555964.609	5165824.239	2841958.227
Mean	-3555962.615	5165821.596	2841956.684
STD	3.673	4.660	2.612

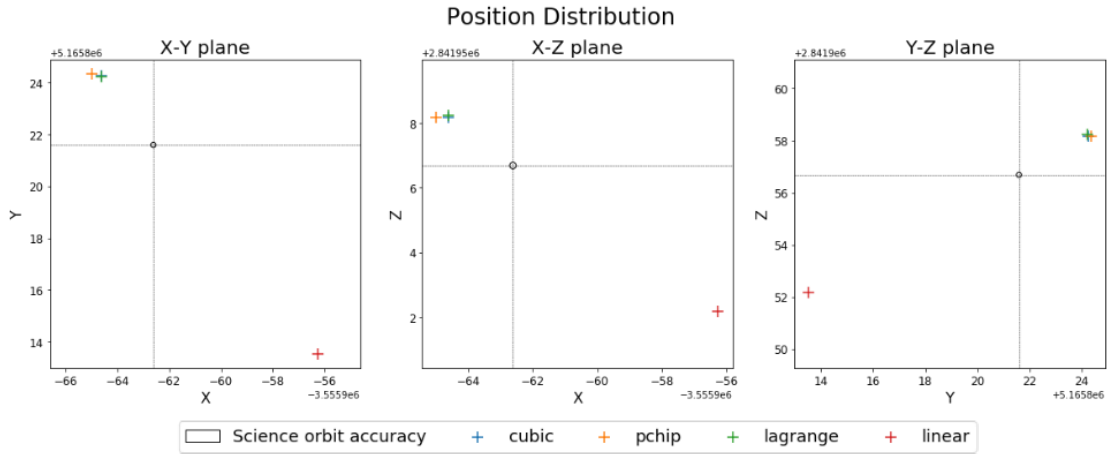

Figure 6. Diagram illustrating the orbit position distribution (4 methods).

Table 2. The interpolated orbit from three interpolation methods.

	X(m)	Y(m)	Z(m)
Cubic	-3555964.607	5165824.265	2841958.182
PCHIP	-3555964.983	5165824.355	2841958.168
Lagrange	-3555964.609	5165824.239	2841958.227
Mean	-3555964.733	5165824.287	2841958.192
STD	0.177	0.050	0.025

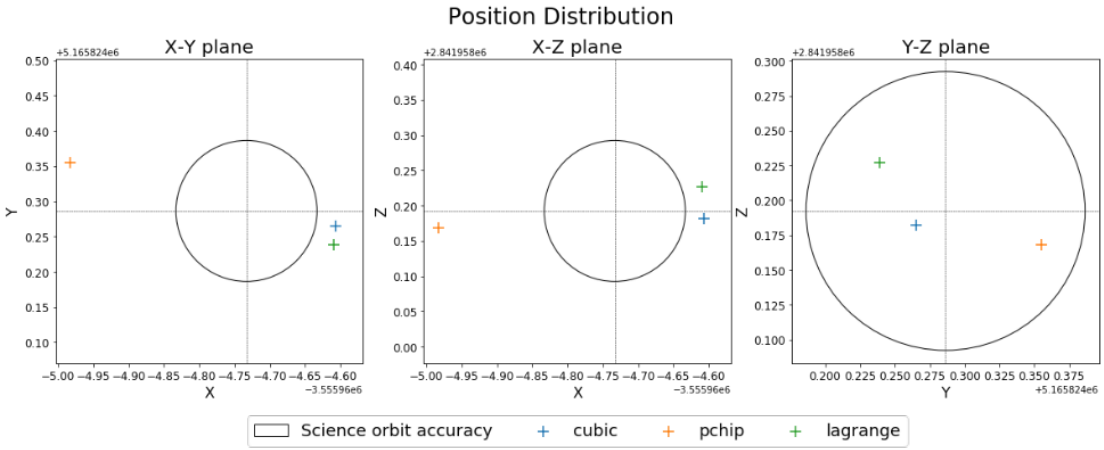

Figure 7. Diagram illustrating the orbit position distribution (3 methods).

3.3 Impact of Interpolation Methods on Perpendicular Baseline

The calculation of the perpendicular baseline in this study involves several steps. Initially, the position of the master orbit is interpolated using the scene center of SAR images. Subsequently, the slave orbit parameters, recorded at intervals of one set every 10 seconds for both TSX and TDX, are interpolated at a finer interval of one set per second. Afterward, the intersection points of the perpendicular lines between the master orbit and slave orbit are computed. As shown in Figure 8, Figure 8(a) represents a schematic diagram of the perpendicular intersection points between the master image's orbit position and the original slave orbit; Figure 8(b) illustrates the schematic diagram of the perpendicular intersection points between the master image's orbit position and the interpolated slave orbit. The blue circles represent the orbit perpendicular intersection points, while the red triangles denote the orbit positions at two timestamps before and after the intersection points. Finally, the perpendicular baseline is determined using the area identity equation.

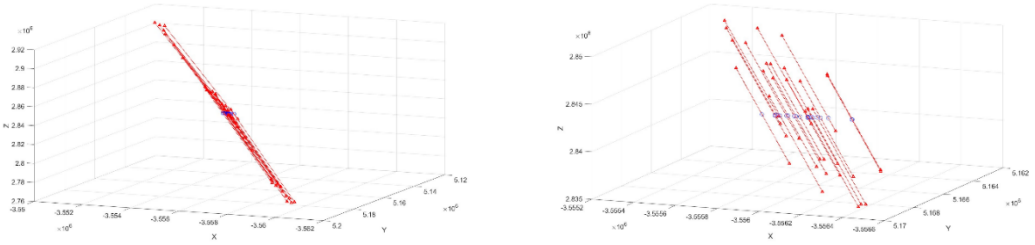

(a) Raw Orbit (b) Interpolated Orbit

Figure 8. Illustration of perpendicular intersection of orbit positions.

3.3.1 External Comparison of Baseline Differences: This study assessed the impact of the four interpolation methods on perpendicular baseline calculations and compared the perpendicular baselines computed by ESA SNAP software (SNAP - ESA Sentinel Application Platform v9.0.0, http://step.esa.int). ESA SNAP is an open-source software. By examining its publicly available source code, one can discern how it computes the coefficients of a third-order polynomial to achieve orbit interpolation, specifically referred to as the normalized cubic polynomial. Regarding the calculation of the perpendicular baseline, the SNAP software computes three crucial measurements: the absolute distance between the master and slave orbits, the parallel baseline, and the viewing angle between the master orbit and the ground point. Through these measurements, the length of the perpendicular baseline can be derived. Specifically, it first calculates the baseline, then determines the parallel baseline by subtracting the distance from the master orbit to the ground point from the distance from the slave orbit to the ground point. Subsequently, it computes the viewing angle and utilizes the Pythagorean theorem to calculate the square of the perpendicular baseline. Finally, the sign of the perpendicular baseline is determined based on the magnitude of the observational angle. Furthermore, it traverses each pixel (line, pixel) of the master image to model baselines as a 2D polynomial of degree 1, aiming to achieve precise estimation of the perpendicular baseline.

This study utilized the TDX image from January 29, 2018, as the master image, and the computational results are presented in Table 3. Among the four interpolation methods, linear interpolation exhibits the largest discrepancy compared to the results derived from ESA SNAP software, with a mean difference of up to -19 meters and a standard deviation of of disagreements exceeding 13 meters. The other three interpolation methods demonstrate closer agreement, with PCHIP yielding the lowest mean difference of -1.492 meters. The lowest standard deviation of baseline differences is observed for cubic interpolation, with a value of 1.313 meters.

Table 3. The results of perpendicular baseline computation.

Satellite	Date	$B_{\perp}(SNAP)$	Error(m)			
			Linear	Cubic	PCHIP	Lagrange
TDX	2018/01/29	0.00	-	-	-	-
TSX	2017/09/08	85.64	-4.026	-2.594	-2.369	-2.583
TSX	2017/10/11	252.09	-28.828	-2.071	-1.663	-2.050
TSX	2017/10/22	166.34	-27.766	-2.081	-1.667	-2.060
TSX	2017/11/02	383.02	-34.236	-1.707	-1.333	-1.687
TSX	2017/11/13	226.35	-32.263	-3.604	-3.208	-3.584
TSX	2017/11/24	337.99	-31.948	-2.384	-1.993	-2.364
TSX	2017/12/05	157.49	-20.906	-2.318	-1.928	-2.299
TSX	2017/12/16	96.92	-13.702	-1.911	-1.555	-1.894
TSX	2018/01/18	187.52	0.801	-1.814	-1.762	-1.811
TSX	2018/05/30	175.26	-34.294	-0.546	-0.180	-0.526
TSX	2018/08/04	191.26	-43.291	-2.696	-2.799	-2.697
TSX	2018/09/06	123.01	-33.653	-2.934	-3.16	-2.943
TSX	2018/12/03	104.46	-15.105	-3.207	-3.357	-3.214
TSX	2018/12/14	144.79	-20.909	-3.786	-3.973	-3.794
TDX	2017/12/27	-110.85	-8.684	-0.151	0.169	-0.136
TDX	2018/01/07	-30.34	0.717	0.690	0.895	0.700
TDX	2018/02/20	-44.90	-1.379	0.476	0.464	0.476
TDX	2018/03/14	-212.90	-3.317	-0.503	-0.529	-0.504
TDX	2018/04/05	-234.64	-2.039	-0.451	-0.224	-0.440
TDX	2018/04/27	-66.84	-25.725	-0.092	0.322	-0.071
		Mean	-19.028	-1.684	-1.492	-1.674
		STD	13.855	1.313	1.383	1.316

3.3.2 Internal Comparison of Baseline Differences

Comparing the perpendicular baseline solutions with those obtained from ESA SNAP, it was observed that when both the master and slave images are from TDX, the error of all interpolation methods is less than 1 meter, except for the linear interpolation. However, when the slave image is from TSX, the error exceeds 1 meter. We performed separate computations for TSX and TDX images, as shown in Table 4. When both the master and slave images are from TSX, the mean difference for cubic and Lagrange interpolation methods is approximately -0.8 meters, with a standard deviation of differences around 1 meter. Conversely,

when both the master and slave images are from TDX, the cubic and Lagrange interpolation methods closely match the results obtained from SNAP, with a mean difference of about 0.19 meters. In short, the variation of TDX's baseline is smaller than TSX's baseline.

Table 4. The error of satellite-wise perpendicular baseline.

Satellite		Difference between the proposed method and ESA SNAP(m)			
		Linear	Cubic	PCHIP	Lagrange
TSX	Mean	4.110	-0.795	-0.934	-0.801
	STD	26.079	1.015	0.996	1.012
TDX	Mean	-4.659	0.188	0.336	0.196
	STD	7.480	1.370	1.483	1.376

3.3.3 Effect of Sampling Interval: The sampling interval for interpolation directly affects the density of timestamps. This section investigates the impact of four different sampling intervals on perpendicular baseline computation. The results, as shown in Table 5, indicate that the linear interpolation method is not affected by the sampling density, while the other three interpolation methods yield perpendicular baselines close to those computed by SNAP when the sampling interval is equal to or less than 1 second.

Table 5. The error of the perpendicular baseline with different interpolation intervals.

Interval(sec)		Difference between the proposed method and ESA SNAP(m)			
		Linear	Cubic	PCHIP	Lagrange
10	Mean	-4.659	-10.720	-10.624	-10.716
	STD	7.480	10.952	10.873	10.949
5	Mean	-4.659	-4.224	-4.135	-4.219
	STD	7.480	3.873	3.784	3.868
1	Mean	-4.659	0.188	0.336	0.196
	STD	7.480	1.370	1.483	1.376
0.5	Mean	-4.659	0.375	0.519	0.382
	STD	7.480	1.272	1.416	1.278

4. CONCLUSIONS AND FUTURE WORKS

In this study, we initially validated the impact of orbit errors on baseline errors through theoretical derivation. Furthermore, we emphasized that orbit interpolation methods directly introduce discrepancies into the orbit, affecting subsequent InSAR applications. In this paper, we also established a procedure for calculating the perpendicular baseline to quantitatively assess the influence of orbit interpolation methods on perpendicular baseline determination. The research findings indicate that orbit errors induced by orbit interpolation significantly impact centimeter-level orbit accuracy in SAR satellites. We further compared the perpendicular baseline calculation results using four interpolation methods and compared them with ESA SNAP. The results indicate that linear interpolation significantly underperforms the other three interpolation methods. Specifically, when both of the master and slave images originate from the same SAR satellite, the cubic interpolation method exhibits a smaller mean difference, approximately -0.8 meters. Additionally, the interpolation sampling interval also directly influences orbit errors. Experiments show that setting the sampling interval for orbit interpolation to one set of orbit parameters every 1-second results in lower mean differences. These research findings provide valuable insights for selecting the most suitable interpolation method to achieve accurate baseline estimation in different scenarios, contributing to the enhancement of InSAR data processing and interpretation. As common interpolation methods such as Trigonometric interpolation and Chebyshev interpolation have not been discussed in this paper, future work will explore additional interpolation techniques. Additionally, the investigation will be extended to analyze the impact of orbit interpolation for InSAR-determined deformation.

ACKNOWLEDGMENTS

This research was partially supported by the Taiwan Space Agency (TASA-S-1120153). The authors would like to thank German Aerospace Center (DLR) for providing TerraSAR-X and TanDEM-X test images.

REFERENCES

Breit, H., Fritz, T., Balss, U., Lachaise, M., Niedermeier, A., & Vonavka, M., 2009. TerraSAR-X SAR processing and products. *IEEE Transactions on Geoscience and Remote Sensing*, 48(2), 727-740.

Chaussard, E., Wdowinski, S., Cabral-Cano, E., & Amelung, F., 2014. Land subsidence in central Mexico detected by ALOS InSAR time-series. *Remote sensing of environment*, 140, 94-106.

Fan, M., Zuo, X., & Tian, J., 2019. Influence of Elevation and Orbit Interpolation on the Accuracy of RD Location Model. In *2019 6th Asia-Pacific Conference on Synthetic Aperture Radar (APSAR)* (pp. 1-4). IEEE.

Fattahi, H., & Amelung, F., 2014. InSAR uncertainty due to orbital errors. *Geophysical Journal International*, 199(1), 549-560.

Feng, Y., & Zheng, Y., 2005. Efficient interpolations to GPS orbits for precise wide area applications. *GPS solutions*, 9, 273-282.

Hackel, S., Gisinger, C., Balss, U., Wermuth, M., & Montenbruck, O. 2018. Long-term validation of TerraSAR-X and TanDEM-X orbit solutions with laser and radar measurements. Remote Sensing, 10(5), 762.

Hanssen, R. F., 2001. *Radar interferometry: data interpretation and error analysis (Vol. 2)*. Springer Science & Business Media.

Hong, S., Choi, Y., Park, I., & Sohn, H. G., 2017. Comparison of orbit-based and time-offset-based geometric correction models for SAR satellite imagery based on error simulation. *Sensors*, 17(1), 170.

Hu, H., & Fang, L., 2009. Interpolation and fitting algorithms for GPS satellite orbit. In *PIAGENG 2009: Remote Sensing and Geoscience for Agricultural Engineering* (Vol. 7491, pp. 61-65). SPIE.

Kang, Y., Lu, Z., Zhao, C., Xu, Y., Kim, J. W., & Gallegos, A. J., 2021. InSAR monitoring of creeping landslides in mountainous regions: A case study in Eldorado National Forest, California. *Remote Sensing of Environment*, 258, 112400.

Lee, E., Hong, S., Choi, Y., Yoo, S., & Sohn, H. G., 2022. Error budget analysis of geocoding and geometric correction for KOMPSAT-5 SAR imagery. *GIScience & Remote Sensing*, 59(1), 1938-1955.

Lepot, M., Aubin, J. B., & Clemens, F. H., 2017. Interpolation in time series: An introductive overview of existing methods, their performance criteria and uncertainty assessment. *Water*, 9(10), 796.

Li, S., Xu, W., & Li, Z., 2022. Review of the SBAS InSAR Time-series algorithms, applications, and challenges. *Geodesy and Geodynamics*, 13(2), 114-126.

Li, Z., Cao, Y., Wei, J., Duan, M., Wu, L., Hou, J., & Zhu, J., 2019. Time-series InSAR ground deformation monitoring: Atmospheric delay modeling and estimating. *Earth-Science Reviews*, 192, 258-284.

Lu, H., Suo, Z., Li, Z., Xie, J., Zhao, J., & Zhang, Q., 2018. InSAR baseline estimation for Gaofen-3 real-time DEM

generation. *Sensors*, 18(7), 2152.

Neta, B., Danielson, D., Clynch, J., & Sagovac, C., 1996. Fast interpolation for global positioning system (GPS) satellite orbits. In *Astrodynamics Conference* (p. 3658).

Osmanoğlu, B., Sunar, F., Wdowinski, S., & Cabral-Cano, E., 2016. Time series analysis of InSAR data: Methods and trends. *ISPRS Journal of Photogrammetry and Remote Sensing*, 115, 90-102.

Pustoshilov, A. S., & Tsarev, S. P., 2017. Universal coefficients for precise interpolation of GNSS orbits from final IGS SP3 data. In *2017 International Siberian Conference on Control and Communications (SIBCON)* (pp. 1-6). IEEE.

Rabbath, C. A., & Corriveau, D., 2019. A comparison of piecewise cubic Hermite interpolating polynomials, Cubics and piecewise linear functions for the approximation of projectile aerodynamics. *Defence Technology*, 15(5), 741-757.

Reigber, C., Xia, Y., Kaufmann, H., Massmann, F. H., Timmen, L., Bodechtel, J., & Frei, M., 1997. Impact of precise orbits on SAR interferometry. In *ERS SAR Interferometry* (Vol. 406, p. 223).

Schenewerk, M., 2003. A brief review of basic GPS orbit interpolation strategies. *GPS solutions*, 6(4), 265-267.

SNAP–ESA Sentinel Application Platform v9.0.0., http://step.esa.int

Teo, T. A., 2011. Bias compensation in a rigorous sensor model and rational function model for high-resolution satellite images. *Photogrammetric Engineering & Remote Sensing*, 77(12), 1211-1220.

Vassilaki, D., & Stamos, A., 2014. Interpolating accurate terrasar-x science orbit data. In *EARSeL 34th Symposium Proceedings*, pp. 2.54-2.62.

Yousif, H., & El-Rabbany, A., 2007. Assessment of several interpolation methods for precise GPS orbit. *The journal of navigation*, 60(3), 443-455.